Functionalized gold nanoparticles as active layer for room temperature vapor-phase elemental mercury detection

Ilaria Fratoddi[a], Sara Cerra[a], Tommaso A. Salamone[a], Raoul Fioravanti[a], Fabio Sciubba[a], Emiliano Zampetti[b], Antonella Macagnano[b], Amanda Generosi[c], Barbara Paci[c], Francesca A. Scaramuzzo[d], Roberto Matassa[e], Giuseppe Familiari[e], Chiara Battocchio[f], Martina Marsotto[f], Paolo Papa[b], Andrea Bearzotti[b]**

a Dpt of Chemistry Sapienza University of Rome, P.le Aldo Moro 5, 00185, Rome Italy

b CNR, Institute of Atmospheric Pollution Research, Via Salaria, km 29.3, Monterotondo, 00015 Rome, Italy

c Consiglio Nazionale delle Ricerche-Istituto di Struttura della Materia (CNR-ISM), Area di Ricerca di Tor Vergata, Via del Fosso del Cavaliere 100, 0013, Rome, Italy

d Dpt of Basic and Applied Sciences for Engineering Sapienza University of Rome, via del Castro Laurenziano,7, 00161 Rome Italy

e Dpt of Anatomical, Histological, Forensic and Orthopaedic Sciences, Section of Human Anatomy, Sapienza University of Rome, Via A. Borelli 50, 00161 Rome, Italy

f Dpt of Sciences, Roma Tre University, via della Vasca Navale 79, 00146 Rome, Italy

Abstract

Nanomaterials such as gold nanoparticles employed as solid-state sensors have attracted attention in recent years due to their ability to detect poisonous elements in the indoor/outdoor environment. Herein, chemoresistive sensors based on gold nanoparticles (AuNPs) functionalized with mixed thiol ligands were tested as sensing materials. Specifically, the electrical response of gold nanoparticles-based sensors was tested against Hg^0_{vap}, H_2S, SO_2, NH_3 and relative humidity (R.H.) at room temperature. Gold nanoparticles samples were synthesized by wet reduction method and then deposited as thin films on suitable interdigitated transducers. Electrical conductivity measurements allowed evaluating a semiconducting behavior of the colloids. Selective and reproducible sensing behavior towards Hg^0_{vap} was observed in the range 0.1-1.0 ng/mL allowing simple and reliable resistive devices to be obtained. An irreversible interaction mechanism, based on the formation of Au-Hg direct bond, was observed in the case of isolated AuNPs samples. Interconnected AuNPs exhibited a reversible behavior as assessed by means of Micro Raman, XRD, XPS, AFM and SEM, UV-Vis and FTIR spectroscopies together with DLS measurements. Broadening of the plasmonic band and increase in mean particle size upon contact with Hg^0_{vap} was observed. The morphological characterization revealed the formation of aggregates after interaction between Hg^0_{vap} and AuNPs. XRD and Micro Raman measurements collected upon the non-exposed and Hg-exposed nanoparticles suggest their structural rearrangement at the surface and the formation of an Au-Hg alloy with Hg mechanically trapped within the bulk material. The simple and cost-effective fabrication of these sensors display prospect in the future as nanodevices for real-time outdoor air quality monitoring.

Introduction

The awareness of the status of environmental contamination is increasingly garnering attention towards global air pollutants[1,2]. Several air pollutants can be detected in the atmosphere, many of which have a great impact on humans and wildlife, and among them, mercury vapors (Hg^0_{vap}), a very volatile element, takes on an important role[3-5]. Over the past decades, the interest towards mercury and its vapors has increased[6], mainly due to its life-threatening consequences on organs such as kidney and liver, combined with neurotoxic effects[7-10]. Mercury cycles are of great importance when it comes to both either prevent or reduce the diffusion of the pollutant. These cycles are related to their sources[11], which are both natural (volcanoes, fires, etc.) and anthropogenic (engines, power plants, etc.)[12,13]. Mercury can be found in many chemical forms in the environment, with methylmercury (MeHg) being the most toxic, due to organisms' absorption and bioaccumulation[14]. MeHg is found in high concentrations in fish, and seafood and recently also in deep oceans fauna[15], hence the consumption of these products represents a health risk[16,17]. However, the most abundant form of mercury in the atmosphere is its inorganic form of gaseous elemental mercury (GEM) or Hg^0_{vap}, which originates from the liquid state due to its high volatility[18]. The volatile vapours of Hg^0_{vap}, due to their long residence time in the atmosphere, estimated from 6 to 24 months[19], have a high global diffusion, with a quite homogeneous concentration ranging from 1.5-1.7 ng/m^3 for the Northern Hemisphere to the 1.1-1.3 ng/m^3 for the Southern Hemisphere[20,21]. Besides the elemental form, mercury is found in the atmosphere in different forms, i.e., gaseous oxidized mercury (GOM) and particle bound mercury (PBM). However, ca. 95% of the Total Gaseous Mercury (TGM) found in the atmosphere is GEM[19,22]. Exposure to GEM has proven adverse effects on human health, mainly because of its rapid absorption in the respiratory tract with negative consequences on the central

nervous system. Although the toxic effect of mercury is dependent on several factors, such as the duration of exposure and the amount of inhaled GEM, short-term/reversible or irreversible health damage can be experienced. For its importance, many methods and instruments aimed to quantify and detect its presence in a certain environment have been developed in the past decades[23]. As it comes, the most common methods to detect the presence of the pollutant exploit or just base their readings on the affinity between noble metals (such as gold and silver) and mercury[24-26]. The interaction between these materials leads to the formation of an amalgam, which is used for the accumulation of mercury, especially at very low concentrations, in sensors based on noble metal film chemoresistors, piezoelectric resonators, quartz microbalances, MOS capacitors and MOSFET's[27-32]. Currently, absorbent gold surfaces are extensively used for both direct and indirect mercury detection. However, these techniques are non-trivial, time consuming and require trained personnel for their use[33]. Most of these methods, in order to overcome cross-interference effects, use a pre-concentrator mercury cartridge - also known as gold trap – prior to desorption and subsequent quantification through different detectors[23]. Severe cross-sensitivity issues caused by common contaminant gases, long operating lifetime, bulky and expensive equipment have greatly increased the demand for alternative detection methods[34]. The use of nanomaterials as sensitive layers is particularly convenient in the detection of mercury vapors due to their high surface area to volume ratio and absorption capacity, which gives an increased efficiency, especially in the presence of low concentrations of pollutants[35-37]. Recently, the use of gold nanoparticles for mercury vapor sensing has been explored, for example as resistive, magnetoelastic and acoustic wave sensors[38]. Accordingly, non-spectroscopic based sensors take advantage of the well-known mercury adsorption/amalgamation process that occurs between Hg^0_{vap} and gold surfaces[39]. The integration of nanomaterials - especially gold nanoparticles - in

the sensing electrode significantly increases the signal-to-background ratio and strongly improves the stability of the sensor when compared to a conventional gold electrode[40]. The advantage of gold nanostructures also lies in the fact that they offer an extensive surface chemistry and can be easily tailored to detect different analytes with an enhancement of selectivity and sensitivity[41-43].

In this work, gold nanoparticles (AuNPs) functionalized with mixed thiol ligands have been employed for the design of solid-state chemoresistive sensors with the aim to elucidate the role of different functionalizing layers. A response of the AuNPs after being exposed to GEM was investigated and evaluated. To investigate their role, different thiol ligands have been selected: an aliphatic one, bearing a sulfonate negatively charged end group (sodium 3-mercapto-1-propanesulfonate, 3MPS), an aromatic thiol (4-bromobenzenethiol, 4BBT), and an aromatic dithiol (4,4'-dithiolbiphenyl, BP) suitable for the formation of interconnected nanoparticles. The modulation of surface functionality was achieved by using mixed hydrophilic and hydrophobic thiols onto the AuNPs surface (i.e., different pairs: AuNPs-1 with 3MPS/4BBT, AuNPs-2 with BP/4BBT, AuNPs-3 with BP/3MPS). This work aims to demonstrate the use of different functionalized gold nanoparticles (AuNPs) as active layers for the realization of a chemosensor able to detect Hg vapors in a wide concentration range without any pre-accumulation/desorption of the analyte. The electrical conductivity measurements for the detection of elemental gaseous mercury were performed with a flow-type device. composed of an interdigitated electrode coated by a drop casted thin film of gold nanoparticles as sensing material. Previous work done using similar device has shown that nanostructure materials based on gold nanoparticles deposited on interdigitated electrodes enhance the sensitivity of resistive sensors with high response[44]. Structural and morphological characterizations studies carried out with Raman, XRD, XPS,

AFM, SEM allowed to define a model of interaction. Time resolved XRD was performed in situ on pristine and previously Hg^0_{vap} exposed AuNPs films, to observe structural reversibility of the sensing material. This device has allowed us to get a directly proportional response to the mercury vapors concentration.

Experimental

Materials

Tetrachloroauric acid ($HAuCl_4 \cdot 3H_2O$), tetraoctylammonium bromide ($N^+[C_8H_{17}]_4Br^-$, TOAB), sodium 3-mercapto-1-propanesulfonate (3MPS, $NaC_3H_7O_3S_2$), 4-bromobenzenethiol (4BBT, BrC_6H_5S), 4,4'-dithiolbiphenyl (BP, $S_2C_{12}H_{10}$), Sodium borohydride ($NaBH_4$), dichloromethane (DCM, CH_2Cl_2), toluene (C_7H_8), ethanol (EtOH, C_2H_6O), N,N-dimethylformamide (DMF, C_3H_7NO), were purchased from Sigma Aldrich and used as received. Deionized water (H_2O_{up}) was obtained with a Zeneer Power I Scholar-UV (Full Tech Instruments) apparatus. A Scilogex centrifuge was used for the purification of the colloidal suspension of AuNPs.

Synthetic procedures

AuNPs functionalized with mixed hydrophilic and hydrophobic thiols were obtained via a Schiffrin-Brust method[45] obtaining the following samples: AuNPs-1 with 3MPS/4BBT, AuNPs-2 with BP/4BBT, AuNPs-3 with BP/3MPS, schematized in **Figure 1**.

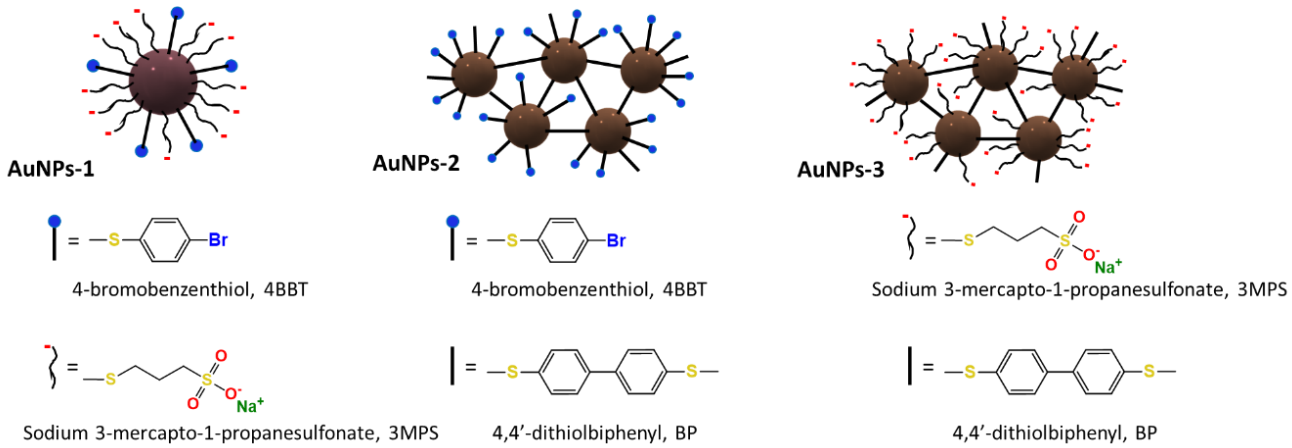

Figure 1. *Chemical structures of AuNPs and used thiols: AuNPs-1 with 3MPS/4BBT, AuNPs-2 with BP/4BBT, AuNPs-3 with BP/3MPS.*

The synthesis of AuNPs-1 is briefly described as an example: firstly, 0.1000 g ($2.54 \cdot 10^{-4}$ mol) of $HAuCl_4 \cdot 3H_2O$ were weighed, dissolved in 5 mL of deionized water, and put in a two-neck round bottom flask under vigorous stirring at room temperature. The reagents were added in the following order: 0.1690 g ($2.54 \cdot 10^{-4}$ mol) of TOAB, dissolved in 10 mL of toluene; 0.1820 g ($1.02 \cdot 10^{-3}$ mol) of 3MPS dissolved in 20 mL of deionized water and finally 0.0480 g ($2.54 \cdot 10^{-4}$ mol) of 4BBT. Sodium borohydride (0.0970 g, $2.54 \cdot 10^{-3}$ mol), dissolved in 5 mL of deionized water was then added under inert atmosphere to reduce the gold Au^{3+} to Au^0. The color of the solution shifted from yellow – $HAuCl_4$ only – to orange with TOAB, white after the ligands were added and finally dark brown following the reduction of the gold. The solution was stirred for three hours before the purification processes. First, the product was purified via extractions in a separating funnel (ca. 5) and the aqueous phase was discarded; the organic phase was then reduced via rotary evaporation. Subsequently, the product was dissolved in ethanol and centrifuged (ca. 15 times) to further eliminate unwanted products and the purified nanoparticles were dissolved in DMF (Yield (wt) 20±8 %). AuNPs-2, and AuNPs-3 samples were obtained with a similar process and dissolved in DCM. The molar ratios between gold and other reagents

can be found in Supporting Information section, together with the main characterization results and reaction schemes (**Figure S1**, **Table S1**).

Structural and spectroscopic characterizations

Absorption spectra of AuNPs dispersed in the appropriate solvent were measured in 1.00 cm optical path quartz cells by using a Cary 100 Varian spectrophotometer. FT-IR spectra were recorded with a Bruker Vertex 70 instrument using KRS-5 cells, in the range 4000-400 cm^{-1} or in ATR configuration on a diamond crystal in the range 4000-600 cm^{-1}; the samples were prepared as cast films. NMR spectra were carried out by using a Bruker Avance 400 spectrometer operating at a frequency of 400.13 MHz for the proton. The compounds were suspended in 0.6 mL of DMF-d_7. Dynamic light scattering (DLS) measurements were carried out on AuNPs suspensions (0.02–0.20 mg/mL in DMF), using a Malvern Zetasizer at temperature of 25.0 ± 0.20°C and using a minimum of ten replicates. All measurements were conducted at least three times and the average value ± standard deviation was reported. FESEM images were obtained using a Zeiss Auriga 405, adopting a voltage level of 7.5 keV and a working distance of 2.5 mm, on freshly prepared films drop casted from DMF solutions (c=1 mg/mL) directly on the metallic sample holder. A variable pressure scanning electron microscopy (VP-SEM, Hitachi SU-3500) supported by dual energy dispersive X-ray spectroscopy detectors (VP-SEM-dEDS) arranged in parallel configuration (Bruker, XFlash® 6|60) able to high sensitivity elemental analysis by their large active area of a 60 mm^2 each was also used. The samples were directly settled onto a carbon planchet stub without conductive coating[46]. All samples were observed at an accelerating voltage depending on the features of the pressure used in the chamber to avoid radiation damage, fatal for EDS spectrum analysis. AFM measurements were carried out in tapping mode with a Multimode™ Veeco model equipped with a Nanoscope IIIa controller and Bruker RTESP-300

probe. AuNPs samples were deposited by drop casting onto a SiO_2 substrate, allowing the aqueous solvent to evaporate in air. Micro Raman measurements were performed on a Renishaw In-Via spectrometer, equipped with a 457 nm laser, in standard confocal mode. The best experimental setup was obtained combining 2400 cm/line grid with a 100X optical enlargement, setting the laser power at 5% of its maximum intensity and acquiring 50 accumulations for t=10 s/point. Same experimental conditions were kept for all measured samples. A Panalytical Empyrean Diffractometer was used to perform XRD in reflection mode using the Kα fluorescence line of a Cu-anode emitting tube as X-ray source (K-α_1 [Å]=1.54060, K-α_2 [Å]=1.54443, K-α_2/K-α_1 Ratio=0.50000). Bragg Brentano configuration was chosen as incident optical pathway (divergent slits ¼° and ½°) and a solid-state hybrid Pix'cel 3D detector, working in 1D linear mode; optimized detection range was determined to be $30°<2\theta<50°$, Step Size [°2θ] = 0.0130 and generator parameters were kept I [mA] = 45 and V [kV] = 40; acquisitions were performed every 12 min to collect in-situ time resolved XRD patterns for an overall 24 hours. XPS measurements were carried out using a homemade instrument, consisting of preparation and analysis UHV chambers separated by a gate valve. The analysis chamber is equipped with a six-degree-of freedom manipulator and a 150 mm mean radius hemispherical electron analyzer with a five-lens output system combined with a 16-channel detector giving a total instrument resolution of 1.0 eV as measured at the Ag $3d_{5/2}$ core level. Samples were introduced in the preparation chamber and left outgassing overnight at a base pressure of about 10^{-8} Torr, before introduction in the analysis chamber. Typical vacuum pressure in the analysis chamber during measurements was in the 10^{-8}–10^{-9} Torr range. The used X-ray radiation is a non-monochromatized Mg Kα (1253.6 eV). The spectra were energy referenced to the C1s signal of aliphatic carbons (BE = 285.0 eV). Curve-fitting analysis of the C1s, S2p, Au4f and Hg4f spectra

was performed using Gaussian profiles as fitting functions, after subtraction of a Shirley-type background. $S2p_{3/2,1/2}$ doublets were fitted by using the same Full Width at Half-Maximum (FWHM) for each pair of components of the same core level, a spin–orbit splitting of 1.2 eV and branching ratios $S2p_{3/2}/S2p_{1/2}=2/1$. For the $Au4f_{7/2,5/2}$ and the $Hg4f_{7/2,5/2}$ doublets, a splitting of 3.7 eV and 4.1 eV respectively, a branch ratio $4f_{7/2}/4f_{5/2}$ of 4/3, and the same FWHM values for both spin−orbit components were used. When several different species were identified in a spectrum, the same FWHM value was set for all individual photoemission bands.

Gas sensing measurements setup

To analyze the electrical and chemical-sensory characteristics, the AuNPs suspensions were deposited by drop casting onto homemade transducers (**Figure S2**). The transducers were based on interdigitated pairs of gold/chromium fingers implemented on passivated silicon substrate by conventional lithography, with the following geometry: fingers width and gaps 20 μm, length 5640 μm, thickness 200 nm[47]. After drop casting of AuNPs onto the transducer, (5 μL of samples suspensions in $CHCl_3$ at concentration 1 mg/mL) films were air dried, inserted into a measurement chamber and connected to a Keithley Model 595 Quasi-static CV Meter. Changes in the flowing current by applying a fixed voltage (0.5 V) were monitored at 20°C by exposure to different Hg^0_{vap} concentrations (range 0.1-1.0 ng/mL). The Hg^0_{vap} quantities, collected from a primary source (TEKRAN 2505) were introduced into the sampling chamber (volume 10 mL) by using a graduated Hamilton syringe withdrawing Hg vapors (Hg vapor pressure is 0.1727 Pa at 293 K/20°C). The vapor was maintained in circulation onto the device by using a micropump (**Figure S2**). To obtain lower quantities of Hg^0_{vap} (range 0.13-50.00 pg/mL), a different apparatus, reported in Fig. S2, was used. The Hg vapor was fluxed onto the device and mixed with dry N_2 using a MKS mass-flow controller and maintaining the total flux at 2000 SCCM

(standard cubic centimeters per minute). Both nitrogen and synthetic air were used as carrier gases without finding any differences in the electrical response of the sensitive layer of AuNPs, as highlighted in the supporting information section. Measurements were also carried out in the presence of different gases to study the selectivity: H_2S (900 ppb, dry), SO_2 (40 ppm, dry), NH_3 (6 ppm, dry) and relative humidity (R.H. 0-50%). I/V and thermal studies were carried out under dry N_2 conditions (2000 SCCM) in the 25-50°C temperature range with a HP 3458A multimeter and a Keithley 230 programmable voltage source.

Results and Discussion

Structural and spectroscopic characterization

Gold nanoparticles functionalized with both hydrophilic and hydrophobic mixed thiols, covalently linked to Au(0) core via Au-S strong covalent bond (ca. 170-210 kJ/mol) were prepared with control towards aggregation[48]. Thanks to the extensive versatility of chemical synthesis of AuNPs, three different colloidal systems were obtained: AuNPs-1 with 3MPS/4BBT, AuNPs-2 with BP/4BBT, AuNPs-3 with BP/3MPS. A negatively charged thiol, 3MPS, was chosen to give hydrophilic character, whereas two hydrophobic aromatic thiols – 4BBT and BP – were employed, the latter being a bifunctional linker which allows the formation of a networked pattern of nanoparticles. A schematic structure of the AuNPs is reported in **Figure 1**. Before exposure to the analyte the nanomaterials were thoroughly characterized. The UV-Visible and DLS results of the pristine AuNPs samples with different capping agents are shown in **Figure 2(a,b)**. **Figure 2a** shows the absorption maximum of AuNPs-1 at about 525 nm, which is attributed to the Localized Surface Plasmon Resonance (LSPR) band typical of isolated gold nanoparticles. In the presence of bifunctional thiols, the SPR absorption band of AuNPs-3 and AuNPs-2 samples broadened and red shifted to 635 nm and 700 nm, respectively.

This result suggested the formation of interconnected nanoparticles due to the intercoupling effects among AuNPs, as already discussed in literature[29]. DLS analyses confirmed the data collected from UV-Vis measurements. **Figure 2b** highlights the presence of a small population of nanoparticles at $<2R_H>$ = 8 ± 2 nm, with regards to the AuNPs-1 sample; DLS spectrum of AuNPs-2, as predicted, shows a population at $<2R_H>$=495 ± 50 nm, whereas AuNPs-3 has a $<2R_H>$=480 ± 40 nm. Further structural characterizations of AuNPs-1, i.e., FTIR and NMR measurements are reported in **Figure S3**.

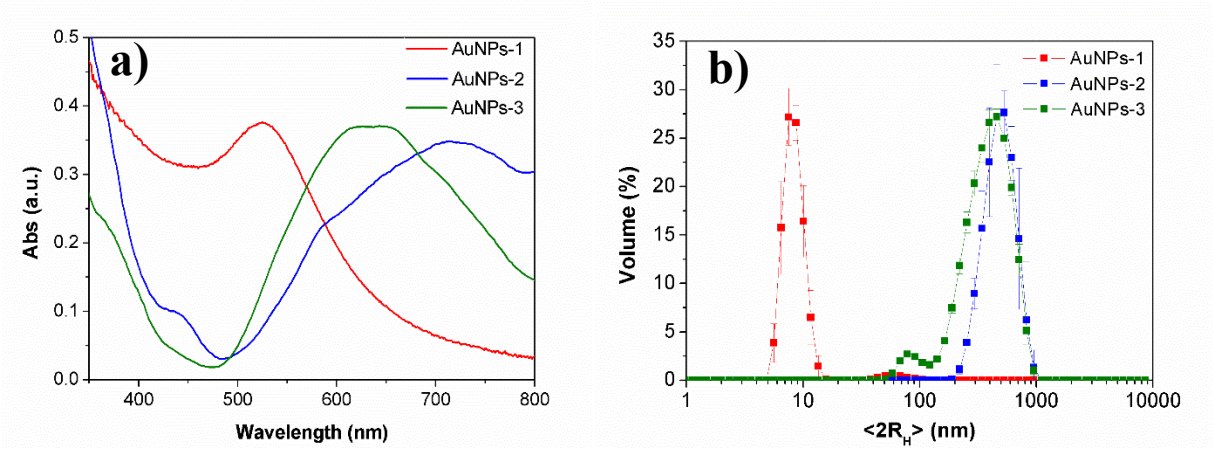

Figure 2. *a) UV-Vis spectra of AuNPs samples in DMF (1 mg/mL). b) AuNPs samples DLS size distribution in DMF (1 mg/mL).*

XPS measurements were carried out on AuNPs-1, AuNPs-2 and AuNPs-3 samples collecting Cs, O1s, S2p, Au4f, Br3d core level signals; a complete collection of Binding Energy (BE) values, Full Width Half Maxima (FWHM), Atomic Ratios and proposed assignments is reported in **Table S2** in the Supporting Information. In particular, the peak fitting analysis carried out on C1s and S2p spectra allowed to confirm the stability of the capping agent molecular structures. C1s spectra (**Figure S4**) show a main component at 285.0 eV that contains contributions from aliphatic, aromatic carbon atoms and C-S groups; a signal at higher BE values (nearly 286.5 eV)

is observed in all samples and attributed to C-Br bonds and C-O arising by contaminants; a last component of very low intensity is observed around 288 eV for AuNPs-1 and AuNPs-2 samples and assigned to carbonyl groups arising by contaminants. Adventitious carbon signals (C-O, C=O species) are usually found on the surface of air exposed samples. S2p signals, reported in **Figure 3**, are interesting because they allow to probe the capping agent-gold nanoparticle chemical interaction[49].

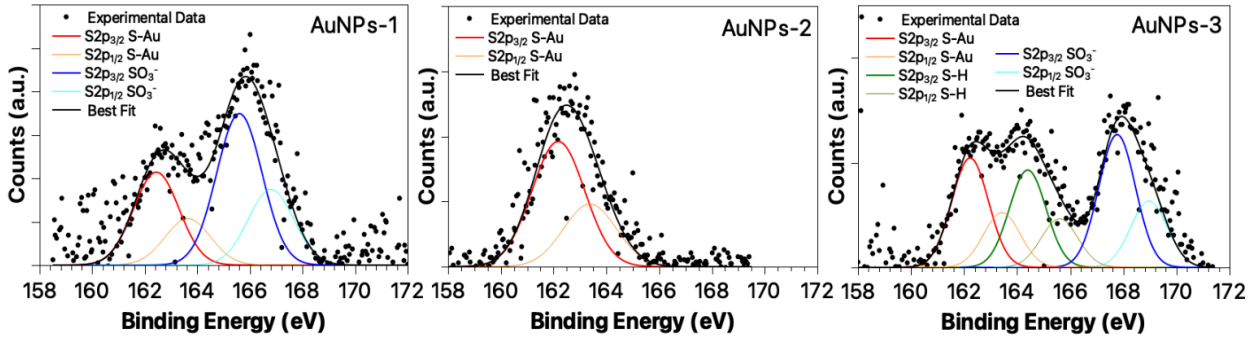

Figure 3. *S2p spectra collected on AuNPs-1, AuNPs-2 and AuNPs-3.*

In sample AuNPs-1 at least two different S atoms can be detected, as expected from the molecular structure of 3MPS and 4BBT ligands: the spin-orbit pair observed at lower BE values is indicative for thiol moieties covalently bonded to gold atoms at the NP surface ($S2p_{3/2}$ component at 162.4 eV BE), while a signal at higher BE is associated with sulphonate —SO_3^- groups of 3MPS ($S2p_{3/2}$ BE = 166 eV), as reported for analogous systems.[49] For AuNPs-2, a single spin-orbit pair is observed and attributed to thiol moieties covalently bonded to gold ($S2p_{3/2}$ BE = 162.2 eV), suggesting that all thiol end-groups of BP and 4BBT are efficiently bonded to gold atoms at the NPs surface. Finally, AuNPs-3 S2p spectrum is similar to the AuNPs-1, but the thiol-like S atoms give rise to two pairs of spin-orbit components indicative for S atoms either covalently bonded to

gold atoms at the NP surface ($S2p_{3/2}$ component at 162.2 eV BE) or physisorbed on the NP surface ($S2p_{3/2}$ component at 164.4 eV BE). The high BE signal associated with sulphonate —SO_3^- groups of 3MPS is also observed, as expected. As for Au4f signals (**Figure S4**), as expected for AuNPs stabilized by thiols, a main component due to metallic gold atoms at the NPs bulk ($Au4f_{7/2}$ BE = 84.0 eV) is observed for all samples. In AuNPs-1 Au4f spectrum a second spin-orbit pair is found at higher BE values ($Au4f_{7/2}$ BE = 85.2 eV) and attributed to partially positively charged gold atoms chemically interacting with thiols at the NP surface, as already observed for similar systems.[49] However, coherently with the DLS and UV-Vis findings about AuNPs mean sizes, Au4f signals collected on AuNPs-2 is barely observable and AuNPs-3 Au4f spectrum is very noisy. This effect is attributed to the very large size (hundreds of nm) of AuNPs-2 and AuNPs-3, giving rise to a lower surface-to-volume ratio.[50]

Sensing mechanism

AuNPs samples were characterized after Hg^0_{vap} exposure to 13 mg/m^3 to evaluate the ligands presence and the possible formation of a direct Au-Hg bond. The optical and morphological responses were assessed by means of UV-visible and FTIR spectroscopies together with dynamic light scattering, XPS, AFM and SEM studies. The UV-Visible spectra of AuNPs-1 sample (1 mg/mL), shown in **Figure 4a** highlights the change in the shape of the plasmonic band after exposure of the gold nanoparticles to mercury, as opposed to the band of AuNPs-1 alone (**Figure 2a**), although no redshift occurs. A shift in the UV-Vis curves was also observed for AuNPs-2 and AuNPs-3 samples, reported in **Figure S5**. The broadening of the plasmonic band is strongly dependent on the increase in mean particle size and polydispersity of the nanoparticles[51]. This assumption can be confirmed by dynamic light scattering. Dynamic light scattering

measurements on AuNPs-1 sample indicate a tendency to aggregation and increase in polydispersity of the AuNPs upon contact with gaseous mercury: before exposure to this analyte, the sample has a mean hydrodynamic diameter of $<2R_H>=8 \pm 2$ nm. This value increases to $<2R_H>=60 \pm 20$ nm after being in contact with Hg^0_{vap} (Fig. 4b). **Figure S5** shows the DLS size distribution of AuNPs-2 and AuNPs-3 after interaction with gaseous mercury. The XPS measurements at Hg4f core level confirmed the presence of metallic mercury in AuNPs-1 after interaction with the analyte (**Figure 4c**)[52]. C1s, S2p and Au4f spectra (reported in **Figure S6**) did not show noticeable modifications, at least within the experimental resolution of this experiment.

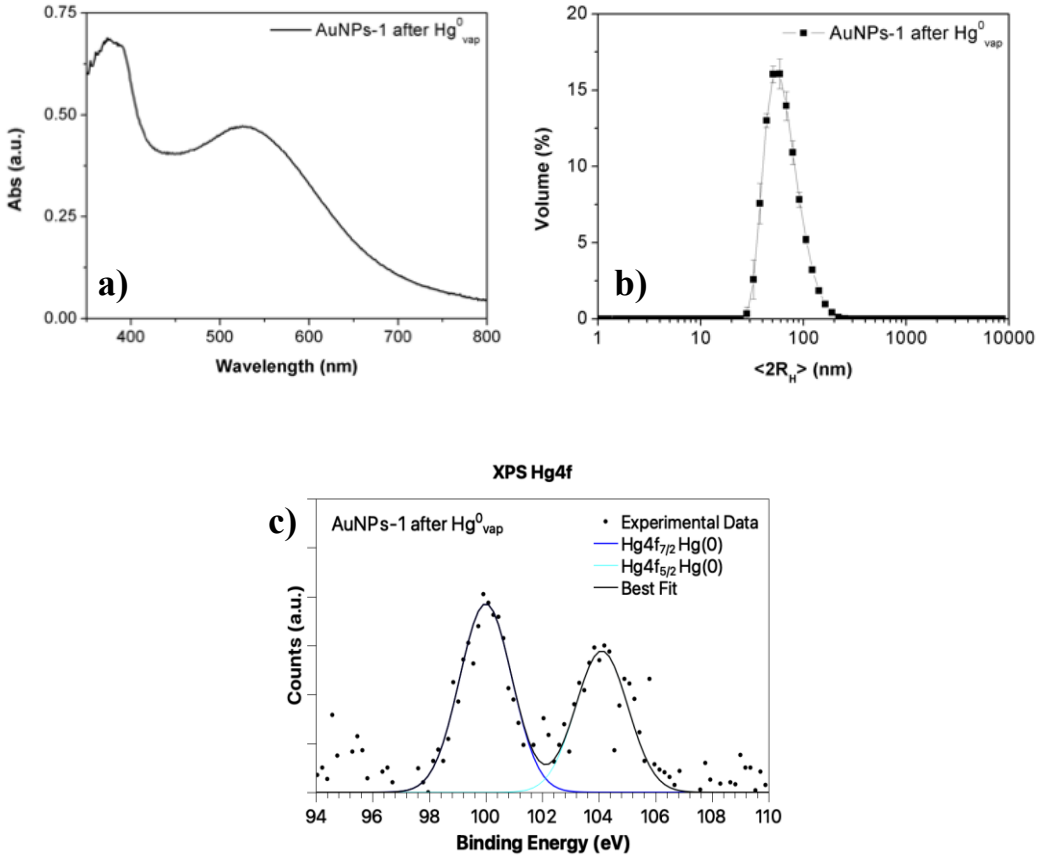

Figure 4. *AuNPs-1 sample in DMF characterisations showing the aggregation and increase in polydispersity after contact with 13 mg/m^3 gaseous mercury (Vapour pressure at 20°C): a) UV-*

vis and b) DLS particle size distribution; c) XPS Hg4f spectrum collected on AuNPs-1 sample exposed to gaseous mercury.

AFM and FESEM analyses were carried out to characterise the colloidal systems from a morphological point of view. As it can be seen, AFM typical images of AuNPs-1, like the one reported in **Figure 5a** showed isolated uniformly distributed AuNPs with maximum height lower than 4 nm before the interaction with Hg^0_{vap}. Exposure to the gaseous analyte leads to a slight but clearly visible increase of the overall particle size distribution, now centred around 5-6 nm and with maximum height up to 9 nm, due to the formation of aggregates, as shown in **Figure 5b**. Statistical analysis performed on randomly selected areas of the sample before and after Hg^0_{vap} exposure highlights the size change (**Figure S7**). Surface morphological image at high magnification of the pristine AuNPs-1 is shown in **Figure 5c**. As-prepared AuNPs were quite spherical, with a particle size in the 5-10 nm range[53]. The exposure of the pristine AuNPs-1 sample to Hg^0_{vap} triggers the coalescence of the nanostructure, which causes the formation of densely packed AuNPs aggregates, in agreement with DLS size distributions and AFM measurements (**Figure 5d**). The dispersive X-ray spectroscopy (EDS) spectrum (**Figure S7**) of the as-prepared AuNPs-1 showed a composition consisting of gold, sulfur and Bromine, due to the aromatic thiol covalently linked on the surface. Similarly, the EDS for AuNPs-1 after Hg^0_{vap} exposure (**Figure S7**) confirmed the presence of elemental mercury. Hence, both morphological and chemical results depict and confirm the interaction between gaseous mercury and the gold colloids.

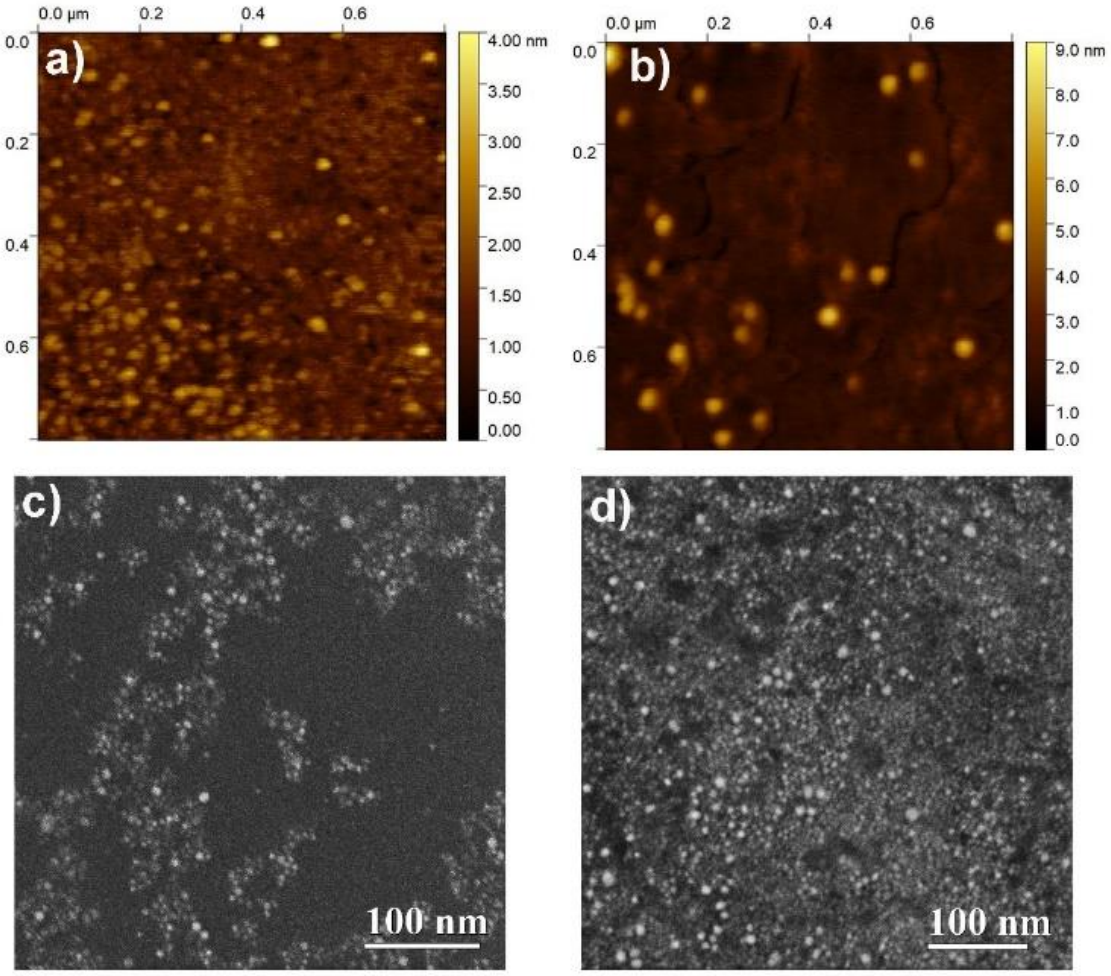

Figure 5. *AFM images on cast deposited AuNPs-1 sample from DMF solutions, a) before and b) after Hg exposure. c) FESEM image of cast deposited AuNPs-1 before Hg exposure. d) FESEM image of cast deposited AuNPs-1 after Hg exposure.*

Preliminary XRD measurements were performed upon the Silicon/SiO2 substrate to detect contributions eventually arising and to further consider them as background in the investigation. As expected, the Si (400) reflection was observed at 2θ (degrees) = 69.000 and labelled in **Figure S8** accordingly to ICCD card Nr. 00-001-0787.54 Subsequently, same experimental conditions were used to compare the unexposed AuNPs-1 sample (black line) with the Hg-long

exposed thin film (red line), and the results are shown in **Figure 6**. As predictable, the substrate Si(400) reflection is the dominant signal and the signals arising from the active material are highlighted in the inset of **Figure 6**. AuNPs were observed as crystalline in both samples, the (111) cubic reflection being detected at 2θ (degrees) = 38.270, according to ICCD Card Nr. 00-001-1174.55 The presence of Au reflections is indicative of the formation of NPs aggregates, since nanostructures as small as 5-10 nm in size are not expected to provide any XRD signal (X-ray amorphous). After prolonged Hg exposure structural modifications were clearly observed, the Au (200) signal at 2θ (degrees) = 44.600 being detected, suggesting a structural rearrangement of the nanoparticles, and most importantly, the formation of an Au-Hg alloy was also observed. Indeed, at 2θ (degrees) = 39.750 a crystalline signal is found, most likely attributed to hexagonal Gold Mercury, ICCD card Nr.: 00-019-0522.

The same samples characterized by XRD, were also studied by means of Micro Raman measurements. It is noteworthy that surface damage induced by laser was not observed thus allowing for accurate measurements to be performed. Due to the presence of embedded AuNPs, Surface Enhanced Raman scattering (SERS) - a technique offering orders of magnitude increases in Raman intensity - was here applied, thus enhancing the signal of molecules absorbed at the metal surface, allowing for accurate chemical investigation and to observe structural modifications occurring as a function of time in air and subsequently under nitrogen forced flux.

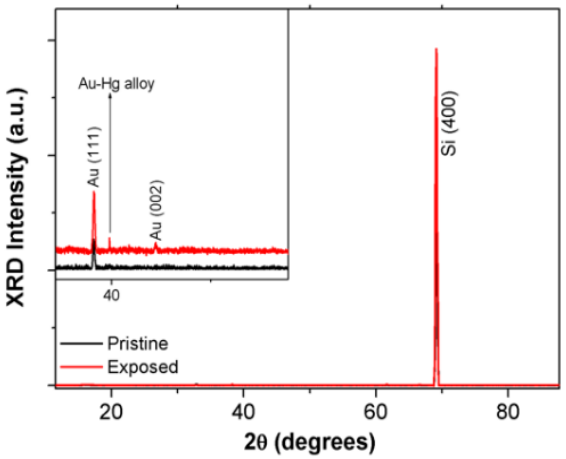

Figure 6. *Comparison of XRD patterns collected upon un-exposed (black line) and Hg-exposed (red line) AuNPs-1 sample. Substrate Si signal is dominant and in the inset the AuNPs reflections are shown, as well as the formation of an Au-Hg complex in the exposed sample.*

The patterns representative of the spectra collected upon Hg-exposed and non-exposed AuNPs-1 sample are reported in **Figure 7** and **Figure S9**, respectively. Both spectra exhibit the strong Si signal (520 cm^{-1}) and overtones, as predictable.

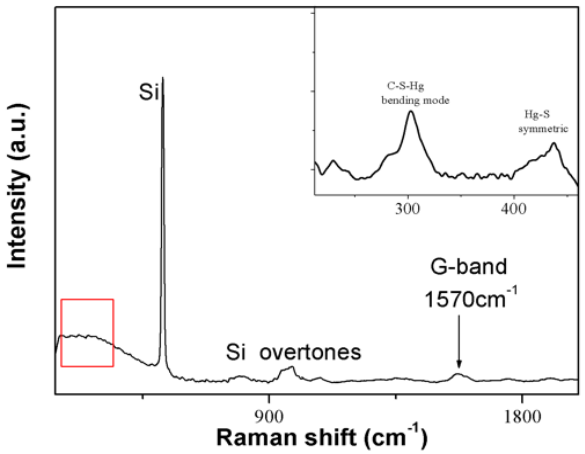

Figure 7. *Raman spectra collected upon Hg°$_{vap}$-exposed AuNPs-1 sample. Substrate Si signal is dominant (520 cm^{-1} and overtones). In the inset the highlight of the low wavenumber region is reported.*

As shown in the inset of **Figure 7**, interestingly the exposed sample exhibits Raman signals arising from the formation of complexes between the functionalized AuNPs and absorbed mercury. In particular, the C-S-Hg ν mode at 302 cm^{-1} and the M_1+M_2 Hg-S vibrational mode at 433 cm^{-1} were detected[56]. Furthermore, the C-C G-band at 1570 cm^{-1} was clearly observed, probably due to a rearrangement of the NPs after Hg uptake. The reversible sensing behavior of AuNPs-3 was established through electrical measurements. Therefore, this sample was further characterized through XRD at different times to evaluate the desorption mechanism of gaseous mercury. Pristine thin AuNPs-3 film deposited onto monocrystalline [100] Si was characterized by XRD in the angular range of interest, to evidence the possible Au nanoparticle crystalline signal. As visible in **Figure 8** (black line), no contribution due to the NPs was observed, indicating that in the present case the NPs aggregates were characterized by nanometric dimensions (less than 20-30 nm), inducing a structural amorphous-like behavior. Subsequently, samples were exposed to Hg vapors for 30 seconds (red line), 90 seconds (blue line) and 3 hours (magenta line), respectively. The presence of the (101) Hg reflection was clearly detected for samples exposed from 90 seconds upward, and labelled accordingly to ICDD Reference code: 00-009-0253, in **Figure 8**[54].

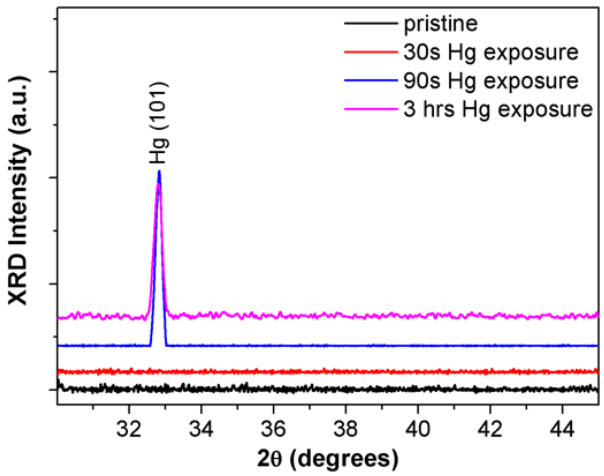

Figure 8. *Sequence of XRD patterns collected upon a pristine AuNPs-3 sample and after different Hg-exposure times. As clearly visible after 90 seconds the Hg absorption is remarkable and structurally detectable.*

Subsequently, in-situ time resolved XRD measurements were performed on 90 seconds exposed sample in air, collecting patterns for 12 minutes each for an overall time of 24 hours, to observe structural reversibility of the sensing material. In **Figure 9a**, the obtained sequence of diffraction patterns is shown and in the inset the Hg crystallinity time evolution is plotted, as obtained by Gaussian fitting procedure of the (101) reflection. As clearly visible, a partial desorption of mercury was observed within the first hour, the (101) crystallinity being reduced by ≈ 50% and subsequently stabilizing itself with no further modification. Indeed, the process was fitted by a first order exponential decay (red line in the inset). Mercury seems to be trapped into the sample, bare simple exposure to air not being capable to enable a complete desorption. To validate this hypothesis, the same sample was subsequently exposed to nitrogen flux, to force mercury desorption from the bulk and same experimental procedure previously described was performed. As clearly evidenced in **Figure 9b**, where the sequence of XRD patterns collected as a function

of N_2 exposure time is shown, within 24 minutes (three curves), superficially trapped mercury was removed bringing the total amount of removed mercury up to 70%. Further 30% was not desorbed after 24 hours of N_2 exposure. This indication validates the hypothesis of mechanically trapped mercury within the bulk material.

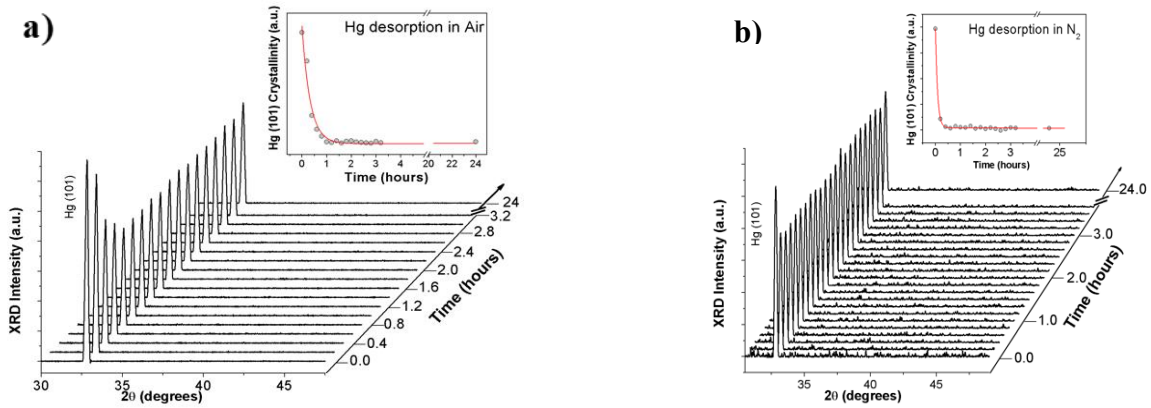

Figure 9. *Sequence of in-situ time resolved XRD patterns on AuNPs-3: (a) collected in air upon a 90 second Hg-exposed film. In the inset the loss of Hg (101) crystallinity associated to the desorption mechanism was evidenced and fitted by a first order exponential decay (red line). Only a partial reset is observed from a structural point of view; (b) collected in N_2 flux on the same sample reported in (a). In the inset the loss of Hg (101) crystallinity associated to the desorption mechanism was evidenced and fitted by a first order exponential decay (red line). A further partial reset was observed from a structural point of view.*

Gas sensing characteristics

Gold nanoparticles are excellent candidates for detecting gaseous mercury, as the interaction with the analyte leads to the formation of an amalgam with gold[27], thus causing a strong variation in the chemical system which can be detected by electrical measurements. Thanks to high surface area to volume ratio and absorption behavior of Hg^0_{vap} on AuNPs, the sensitivity of

the system can experience a synergic enhancement. Moreover, the role of the functionalizing thiols can be fundamental to drive the interaction, with a fine control on the aggregation equilibria[29]. Some of the literature papers that report about metal nanostructured sensors for mercury detection mainly detect Hg^{2+} ions in tap, waterways, and sea water samples[58,59]. However, mercury ions can be converted into vapor form which is the main root for the respiratory and immune system failure in humans[7,8]. With the aim of obtaining simple and cost-effective gold nanoparticles-based sensors, the synthesized colloidal samples were tested as resistive Hg^0_{vap} gas sensors.

To assess the electrical behavior of the selected AuNPs, electrical measurements were carried out on AuNPs-1, AuNPs-2, AuNPs-3 films. As confirmed by the I *vs.* V and I *vs.* T measurements (reported in **Figure S10**), a semiconducting behavior was observed with E_a measured in the case of AuNPs-1 equal to 0.108 eV, in good agreement between the studied samples and literature data on AuNPs[57]. In order to investigate the sensor sensitivity and selectivity towards Hg^0_{vap} at room temperature, the responses of the three AuNPs samples to various gases were investigated. AuNPs-2 and AuNPs-3 showed the highest sensitivity towards Hg^0_{vap}, being able to detect quantities as low as 10 pg/m^3, but the most effective and stable response was obtained with AuNPs-1. Indeed, in the case of AuNPs-1 sample, a reproducible response to small amounts (1 $\mu g/m^3$) of Hg^0_{vap} was observed with a time response of less than 30 seconds, as reported in **Figure 10a**.

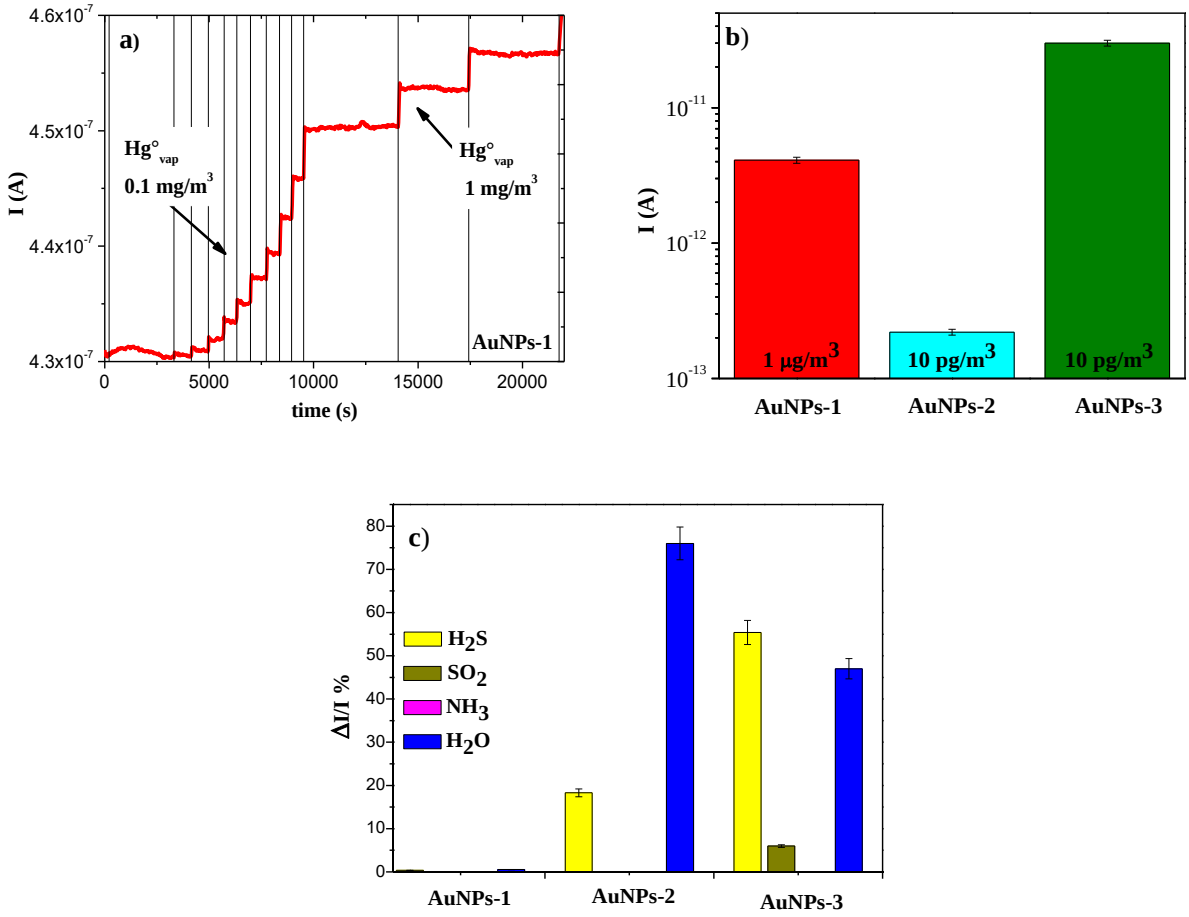

Figure 10. *a) Electrical response towards increasing amounts of Hg^0_{vap} with AuNPs-1 sample (steps from 0.1 mg/m^3 to 1 mg/m^3; T 25°C, R.H. 24%); b) Comparison of the electrical responses of AuNPs-1 (red), AuNPs-2 (ciano) and AuNPs-3 (green) samples towards Hg^0_{vap} concentrations; c) H_2S (900 ppb), SO_2 (40 ppm), NH_3 (6 ppm), relative humidity (R.H. 50%) responses of AuNPs-1, AuNPs-2 and AuNPs-3 samples. (applied voltage 0.5 V).*

It is remarkable that a cumulative, non-reversible effect was obtained with sensitivity to low mercury quantities in the 0.1-1.0 ng/mL range. It is noteworthy that a response was also observed in the case of AuNPs-2 and AuNPs-3 films, with a reversible response but with different sensitivity (see **Figure 10b** and **Figure S11**). Sensor membrane based on AuNPs-3 sample also

showed a reversible signal. These data were compared with our preliminary results of homologous AuNPs stabilized with single thiols.[29] These materials showed to be efficient absorbers and were also electrically tested towards Hg^0_{vap}, showing no response. Therefore, AuNPs-1 and AuNPs-3 were further characterized to assess the sensing mechanism. For sensing practical application, the gas sensing properties towards H_2S, SO_2, dry NH_3 and relative humidity (R.H.) were also investigated. A higher selectivity to small amounts of Hg^0_{vap} was obtained in the case of AuNPs-1, which showed only a minimal to no response to H_2S, SO_2 and NH_3. AuNPs-2 showed little to no response towards SO_2 and NH_3, but the conductivity of the sample increased significantly when exposed to H_2S and R.H. AuNPs-3 was responsive towards H_2S and SO_2 (**Figure S12**) while it was insensitive to the presence of NH_3 (see **Figure 10c**, **Table S3**).

Conclusions

Gold nanoparticles capped with mixed hydrophilic and hydrophobic thiols were prepared via a simple and inexpensive two-phase method and tested as sensing materials for the detection of toxic gases. Solid-state sensors were obtained through deposition of thin film gold nanoparticles on interdigitated electrodes and their response against Hg^0_{vap} and other possible contaminants, such as H_2S, SO_2, NH_3 and relative humidity (R.H.), was studied. Gas-sensing measurements have shown that these materials were sensitive and selective towards gaseous Hg^0_{vap} at room temperature. Herein, functionalization of the AuNPs plays a pivotal role in which the appropriate selection of thiol ligands can provide a detection system with different selectivity and sensitivity. Indeed, depending on the nature of the colloidal samples, i.e., isolated/interconnected AuNPs, different behaviors can be observed. Irreversible response towards 1 $\mu g/m^3$ of Hg^0_{vap} was

observed in the case of isolated nanoparticles AuNPs-1 sample, due to a structural rearrangement of the nanoparticles and the formation of an Au-Hg alloy with Hg mechanically trapped within the bulk material, as evidenced by XRD and Micro Raman measurements. Interconnected AuNPs-2 and AuNPs-3 samples showed a reversible behavior to lower concentrations of gases, due to the nature of the nanostructure as the AuNPs network does not allow a proper interaction between Hg^0_{vap} and the surface. However, the interconnected samples did not exhibit a selective response. Structural and morphological characterizations allowed to focus on the interaction mechanism and to understand how the AuNPs can detect Hg^0_{vap} in the 0.1-1.0 ng/mL range. Optical measurements together with DLS, AFM and SEM analyses evidenced aggregation phenomena. Overall, our results indicate the use of mixed thiol ligands functionalized AuNPs, showing a selective and reproducible sensing behavior, as a very promising cost-effective strategy in developing chemoresistive sensor for elemental gaseous mercury detection.

Supporting Information

The following files are available free of charge. The Supporting Information contains schemes for the synthesized AuNPs systems (**Figure S1**), schematic diagrams of the electrical measurements (**Figure S2**), FTIR spectra of the AuNPs systems (**Figure S3**), XPS measurements of AuNPs systems (**Figure S4**), UV-Vis and DLS spectra of the sensing devices (**Figure S5**), XPS measurements of AuNPs after interaction (**Figure S6**), AFM and EDS measurements (**Figure S7**), XRD pattern of the silicon/silicon oxide substrate (**Figure S8**), Raman spectra collected upon un-exposed AuNPs-1 sample (**Figure S9**), I/V graphs (**Figure S10**), electrical response to analytes (**Figures S11, S12**), Experimental parameters for the synthesis and main characterizations (**Table S1**), C1s, S2p, Au4f and Hg4f XPS data (assignments, BE, FWHM, Atomic Percentages) of AuNPs systems (**Table S2**), Electrical response of AuNPs towards different analytes (**Table S3**).

AUTHOR INFORMATION

Corresponding Author

*Ilaria Fratoddi, ilaria.fratoddi@uniroma1.it; Andrea Bearzotti, a.bearzotti@iia.cnr.it

Author Contributions

The manuscript was written through contributions of all authors. All authors have given approval to the final version of the manuscript.

Acknowledgements

The authors are grateful to Mr. Marco Guaragno (CNR-ISM) for his technical support with X-ray experiments. IF gratefully acknowledges Ateneo funding grants 2017, 2018 and 2019.

References

[1] M. Shahid, B. Pourrut, C. Dumat, M. Nadeem, M. Aslam, E. Pinelli, Heavy-metal-induced reactive oxygen species: phytotoxicity and physicochemical changes in plants, Rev. Environ. Contam. T. 232 (2014), 1-44. Doi: https://doi.org/10.1007/978-3-319-06746-9_1.

[2] Z. Rahman, V.P. Singh, The relative impact of toxic heavy metals, The relative impact of toxic heavy metals (THMs) (arsenic (As), cadmium (Cd), chromium (Cr)(VI), mercury (Hg), and lead (Pb)) on the total environment: an overview, Environ. Monit. Assess. 191 (2019), 419. Doi: https://doi.org/10.1007/s10661-019-7528-7.

[3] C.O.R. Okpala, G. Sardo, S. Vitale, G. Bono, A. Arukwe, Hazardous properties and toxicological update of mercury: From fish food to human health safety perspective, Crit. Rev. Food Sci. Nutr. 58 (2018), 1986-2001. Doi: https://doi.org/10.1080/10408398.2017.1291491.

[4] D. O'Connor, D. Hou, Y.S. Ok, J. Mulder, L. Duan, Q. Wu, S. Wang, F.M.G. Tack, J. Rinklebe, Mercury speciation, transformation, and transportation in soils, atmospheric flux, and implications for risk management: A critical review, Environ. Int. 126 (2019), 747-761. Doi: https://doi.org/10.1016/j.envint.2019.03.019.

[5] F. Khan, S. Momtaz, M. Abdollahi, The relationship between mercury exposure and epigenetic alterations regarding human health, risk assessment and diagnostic strategies, J. Trace Elem. Med. Bio. 52 (2019), 37-47. Doi: https://doi.org/10.1016/j.jtemb.2018.11.006.

[6] A. Carpi, Y.-F. Chen, Gaseous elemental mercury as an indoor air pollutant, Environ. Sci. Technol. 35 (2001), 4170-4173. Doi: https://doi.org/10.1021/es010749p.

[7] S. Hussain, A. Atkinson, S.J. Thompson, A.T. Khan, Accumulation of mercury and its effect on antioxidant enzymes in brain, liver, and kidneys of mice, J. Environ. Sci. Heal. B 34 (1999), 645-660. Doi: https://doi.org/10.1080/03601239909373219.

[8] K.M. Rice, E.M. Walker Jr., M. Wu, C. Gillette, E.R. Blough, Environmental mercury and its toxic effects, J. Prev. Med. Public Health 47 (2014), 74-83. Doi: http://dx.doi.org/10.3961/jpmph.2014.47.2.74.

[9] G. Qiu, Total mercury and methylmercury accumulation in wild plants grown at wastelands composed of mine tailings : Insights into potential candidates for phytoremediation, Environ. Pollut. 239 (2018), 757-767. Doi: https://doi.org/10.1016/j.envpol.2018.04.105.

[10] G. Bjørklund, M. Dadar, J. Mutter, J. Aaseth, The toxicology of mercury: Current research and emerging trends, Environ. Res. 159 (2017), 545-554. Doi: https://doi.org/10.1016/j.envres.2017.08.051.

[11] C.J. Lin, S.O. Pehkonen, The chemistry of atmospheric mercury: A review, Atmos. Environ. 33 (1999), 2067-2079. Doi: https://doi.org/10.1016/S1352-2310(98)00387-2.

[12] D.G. Streets, H.M. Horowitz, D.J. Jacob, Z. Lu, L. Levin, A.F.H. Schure, E.M. Sunderland, Total mercury released to the environment by human activities, 51 (2017), 5969-5977. Doi: https://doi.org/10.1021/acs.est.7b00451.

[13] E.G. Pacyna, J.M. Pacyna, K. Sundseth, J. Munthe, K. Kindbom, S. Wilson, F. Steenhuisen, P. Maxson, Global emission of mercury to the atmosphere from anthropogenic sources in 2005 and projections to 2020, Atmos. Environ. 44 (2010), 2487-2499. Doi: https://doi.org/10.1016/j.atmosenv.2009.06.009.

[14] P. Li, B. Du, H.M. Chan, X. Feng, B. Li, Mercury bioaccumulation and its toxic effects in rats fed with methylmercury polluted rice, Sci. Total Environ. 633 (2018), 93-99. Doi: https://doi.org/10.1016/j.scitotenv.2018.03.185.

[15] R. Sun, J. Yuan, J.E. Sonke, Y. Zhang, T. Zhang, W. Zheng, S. Chen, M. Meng, J. Chen, Y. Liu, X. Peng, C.Liu, Methylmercury produced in upper oceans accumulates in deep Mariana Trench fauna. Nat. Commun .11 (2020), 3389. Doi: https://doi.org/10.1038/s41467-020-17045-3.

[16] D.G. Buck, D.C. Evers, E. Adams, J. Digangi, B. Beeler, J. Samánek, J. Petrlik, M.A. Turnquist, O. Speranskaya, K. Regan, S. Johnson, A global-scale assessment of fish mercury concentrations and the identification of biological hotspots, Sci. Total Environ. 687 (2019), 956-966. Doi: https://doi.org/10.1016/j.scitotenv.2019.06.159.

[17] Y. Wang, M. Gao, C. Liao, F. Yu, L. Chen A sulfydryl-based near-infrared ratiometic fluorescent probe for assessment of acute/chronic mercury exposure via associated determination of superoxide anion and mercury ion in cells and in vivo, Sens. Actuat. B Chem. 301 (2019), 127038. Doi: https://doi.org/10.1016/j.snb.2019.127038.

[18] United Nations Environment Programme, The global atmospheric mercury assessment: sources, emissions and transport, UNEP-Chemicals Branch (2008) 13-62, http://www.chem.unep.ch/mercury/Atmospheric_Emissions/UNEP%20SUMMARY%20REPORT%20-%20final%20for%20WEB%20Dec%202008.pdf

[19] L. Zhang, S.X. Wang, L. Wang, J.M. Hao, Atmospheric mercury concentration and chemical speciation at a rural site in Beijing, China: implications of mercury emission sources, Atmos. Chem. Phys. 13 (2013), 10505-10516. Doi: https://doi.org/10.5194/acp-13-10505-2013.

[20] S. Lindberg, R. Bullock, R. Ebinghaus, D. Engstrom, X.B. Feng, W. Fitzgerald, N. Pirrone, E. Prestbo, C. Seigneur, A synthesis of progress and uncertainties in attributing the sources of mercury in deposition, AMBIO 36 (2007), 19-32. Doi: https://doi.org/10.1579/0044-7447(2007)36[19:ASOPAU]2.0.CO;2.

[21]X. Fu, X. Feng, J. Sommar, S. Wang, A review of studies on atmospheric mercury in China, Sci. Total Environ. 421-422 (2012), 73-81. Doi: https://doi.org/10.1016/j.scitotenv.2011.09.089.

[22] W.H. Schroeder, J. Munthe, Atmospheric mercury - An overview, Atmos. Environ. 32 (1998), 809-822. Doi: https://doi.org/10.1016/S1352-2310(97)00293-8.

[23] M.S. Gustin, H.M. Amos, J. Huang, M.B. Miller, K. Heidecorn, Measuring and modeling mercury in the atmosphere: a critical review, Atmos. Chem. Phys. 15 (2015), 5697-5713. Doi: https://doi.org/10.5194/acp-15-5697-2015.

[24] H. Okamoto, T.B. Massalski, The Au-Hg (Gold-Mercury) system, Bull. Alloy Phase Diagr. 10 (1989), 50-58. Doi: https://doi.org/10.1007/BF02882176.

[25] M. Levlin, E. Ikävalko, T. Laitinen, Adsorption of mercury on gold and silver surfaces, Fresenius. J. Anal. Chem. 365 (1999), 577-586. Doi: https://doi.org/10.1007/s002160051526.

[26] I. Kocemba, M.I. Szynkowska, E. Maćkiewicz, J. Góralski, J. Rogowski, R. Pietrasik, P. Kula, Ł. Kaczmarek, K. Jóźwik, Adsorption of gas-phase elemental mercury by sulphonitrided steel sheet. Effect of hydrogen treatment, J. Haz. Mat. 368 (2019), 722-731. Doi: https://doi.org/10.1016/j.jhazmat.2019.01.102.

[27] M. George, W. Glaunsinger, The electrical and structural properties of gold films and mercury-covered gold films, Thin Solid Films 245 (1994), 215-224. Doi: https://doi.org/10.1016/0040-6090(94)90903-2.

[28] T. Kobiela, B. Nowakowski, R. Duś, The influence of gas phase composition on the process of Au-Hg amalgam formation, Appl. Surf. Sci. 206 (2003), 78-89. Doi: https://doi.org/10.1016/S0169-4332(02)01190-X.

[29] A. Bearzotti, P. Papa, A. Macagnano, E. Zampetti, I. Venditti, R. Fioravanti, L. Fontana, R. Matassa, G. Familiari, I. Fratoddi. Environmental Hg vapours adsorption and detection by using

functionalized gold nanoparticles network, J. Environm. Chem Eng. 6 (2018), 4706-4713. Doi: https://doi.org/10.1016/j.jece.2018.07.013.

[30] A. Chalkidis, D. Jampaiah, P.G. Hartley, Y.M. Sabri, Mercury in natural gas streams: A review of materials and processes for abatement and remediation, J. Haz. Mater. 382 (2020), 121036. Doi: https://doi.org/10.1016/j.jhazmat.2019.121036.

[31] G. Lu, L. Hou, T. Zhang, J. Liu, H. Shen, C. Luo, Q. Gong, Plasmonic sensing via photoluminescence of individual gold nanorod, J. Phys. Chem. C. 116 (2012), 25509-25516. Doi: https://doi.org/10.1021/jp309450b.

[32] B. Lay, A.E. Kandjani, M.H. Amin, K.M.M. Kabir, S.J. Ippolito, Y.M. Sabri, S.K. Bhargava, Galvanic replacement of colloidal monolayer crystal on a QCM device for selective detection of mercury vapor, Sens. Actuat. B Chem. 250 (2017), 383–392. Doi: https://doi.org/10.1016/j.snb.2017.04.166.

[33] E.B. Santos, S. Ferlin, A.H. Fostier, I. O. Mazali, Using Gold Nanoparticles as Passive Sampler for Indoor Monitoring of Gaseous Elemental Mercury, J. Braz. Chem. Soc. 28 (2016), 1-7. Doi: https://doi.org/10.21577/0103-5053.20160290.

[34] K.M. M. Kabir, S. J. Ippolito, A. E. Kandjani, Y. M Sabri, S. K Bhargava, Nano-engineered surfaces for mercury vapor sensing: Current state and future possibilities, Trends Analyt. Chem. 88 (2017), 77-99. Doi: https://doi.org/10.1016/j.trac.2016.12.009.

[35] A. Macagnano, P. Papa, J. Avossa, V. Perri, M. Marelli, F. Sprovieri, E. Zampetti, F. De Cesare, A. Bearzotti, N. Pirrone, Passive Sampling of Gaseous Elemental Mercury Based on a Composite TiO_2 NP/AuNP Layer, Nanomaterials 8 (2018), 798. Doi: https://doi.org/10.3390/nano8100798.

[36] A.G. Memon, X. Zhou, J. Liu, R. Wang, L. Liu, B . Yu, M. He, H. Shi, Utilization of unmodified gold nanoparticles for label-free detection of mercury (II): Insight into rational design of mercury-specific oligonucleotides, J. Hazard. Mater. 321 (2017), 417–423. Doi: https://doi.org/10.1016/j.jhazmat.2016.09.025.

[37] C. Schopf, A. Martín, D. Iacopino, Plasmonic detection of mercury via amalgam formation on surface-immobilized single Au nanorods, Sci. Technol. Adv. Mater. 18 (2017), 1-8. Doi: https://doi.org/10.1080/14686996.2016.1258293.

[38] N. Lerner, T. Ohaion-Raz, O. Zeiri, Improving the properties of a gold nanoparticle barium sensor through mixed-ligand shells, Talanta 208 (2020), 120370. Doi: https://doi.org/10.1016/j.talanta.2019.120370.

[39] T. Hou, M. Chen, G.W. Green, R.G. Horn, Mercury Vapor Sorption and Amalgamation with a Thin Gold Film, ACS Appl. Mater. Interfaces 7 (2015) 23172–23181. doi: 10.1021/acsami.5b07002.

[40] J. H. Bergantin Jr., A.P.C. Veranga, D. R. B. Albano, F.B. Sevilla III, Gold thin film chemiresistor sensor for gaseous elemental mercury, J. Appl. Sci. 16 (2017), 19-25. Doi: https://doi.org/10.14416/j.appsci.2017.10.S03.

[41] M. Cottat, C. D'andrea, R. Yasukuni, N. Malashikhina, R. Grinyte, N. Lidgi-Guigui, B. Fazio, A. Sutton, O. Oudar, N. Charnaux, V. Pavlov, A. Toma, E. Di Fabrizio, P.G. Gucciardi, M. Lamy De La Chapelle, High Sensitivity, High Selectivity SERS Detection of MnSOD Using Optical Nanoantennas Functionalized with Aptamers, J. Phys. Chem. C 119 (2015), 15532-15540. Doi: https://doi.org/10.1021/acs.jpcc.5b03681.

[42] N. Wang, Y. Liu, Y. Li, Q. Li, M. Xie, Fluorescent and colorimetric sensor for Cu^{2+} ion based on formaldehyde modified hyperbranched polyethylenimine capped gold nanoparticles, Sens. Actuat. B Chem. 255 (2018), 78-86. Doi: https://doi.org/10.1016/j.snb.2017.08.035.

[43] X. Chen, S. Zhao, P. Zhou, B. Cui, W. Liu, D. Wei, Y. Shen, Room-temperature NO_2 sensing properties and mechanism of CuO nanorods with Au functionalization, Sens. Actuat. B. Chem. 328 (2021), 129070. Doi: https://doi.org/10.1016/j.snb.2020.129070.

[44] I. Venditti, I. Fratoddi, M.V. Russo, A. Bearzotti, A nanostructured composite based on polyaniline and gold nanoparticles: synthesis and gas sensing properties, Nanotechnology 24 (2013), 155503. Doi: https://doi.org/10.1088/0957-4484/24/15/155503.

[45] L.M. Liz-Marzán, Gold nanoparticle research before and after the Brust–Schiffrin method, Chem. Commun. 49 (2013), 16-18. Doi: https://doi.org/10.1039/c2cc35720h.

[46] M. Bossù, R. Matassa, M. Relucenti, F. Iaculli, A. Salucci, G. Di Giorgio, G. Familiari, A. Polimeni, S. Di Carlo, Morpho-Chemical Observations of Human Deciduous Teeth Enamel in Response to Biomimetic Toothpastes Treatment, Materials 11 (2020), 1803. Doi: https://doi.org/10.3390/ma13081803.

[47] I. Fratoddi, P. Altamura, A. Bearzotti, A. Furlani, M.V. Russo. Electrical and morphological characterization of poly(monosubstituted)acetylene based membranes: application as humidity and organic vapors sensors, Thin Solid Films 458 (2004), 292-298. Doi: https://doi.org/10.1016/j.tsf.2003.12.065.

[48] E. Pensa, E. Cortés, G. Corthey, P. Carro, C. Vericat, M. Fonticelli, G. Benítez, A. Rubert, R. Salvarezza, The Chemistry of the Sulfur–Gold Interface: In Search of a Unified Model. Acc. Chem. Res. 45 (2012), 1183-1192. Doi https://doi.org/10.1021/ar200260p.

[49] L. Carlini, C. Fasolato, P. Postorino, I. Fratoddi, I. Venditti, G. Testa, C. Battocchio, Comparison between Silver and Gold Nanoparticles Stabilized with Negatively Charged Hydrophilic Thiols: SR-XPS and SERS as Probes for Structural Differences and Similarities, Coll. Surf. A, 532 (2017), 183-188. doi:10.1016/j.colsurfa.2017.05.045.

[50] F. Mochi, L. Burratti, I. Fratoddi, I. Venditti, C. Battocchio, L. Carlini, G. Iucci, M. Casalboni, F. De Matteis, S. Casciardi, S. Nappini, I. Pis, P. Prosposito, Plasmonic Sensor Based on Interaction between Silver Nanoparticles and Ni2+ or Co2+ in Water. Nanomaterials 2018, 8(7), 488; https://doi.org/10.3390/nano8070488

[51] M.S. Frost, M.J. Dempsey, D.E. Whitehead, The Response of Citrate Functionalised Gold and Silver Nanoparticles To The Addition of Heavy Metal Ions, Colloids Surf. A: Physicochem. Eng. Asp. 518 (2017), 15-24. Doi: https://doi.org/10.1016/j.colsurfa.2016.12.036.

[52] P. Prosposito, L. Burratti, A. Bellingeri, G. Protano, C. Faleri, I. Corsi, C. Battocchio, G. Iucci, L. Tortora, V. Secchi, S. Franchi, I. Venditti, Bifunctionalized silver nanoparticles as Hg2+ plasmonic sensor in water: synthesis, characterizations and ecosafety, Nanomaterials 2019, 9(10), 1353; https://doi.org/10.3390/nano9101353

[53] R. Matassa, G. Familiari, E. Battaglione, C. Sibilia, G. Leahu, A. Belardini, I. Venditti, L. Fontana, and I. Fratoddi, Electron Microscopy Reveals Layered Architecture of Individual Gold Nanoparticles Self-Anchored by Fluorescence Monomers, Nanoscale 8 (2016), 18161-18169. Doi: https://doi.org/10.1039/C6NR06260A.

[54] C.S. Barrett, The Structure of Mercury at Low Temperatures, Acta Cryst. 10 (1957), 58-60. Doi: https://doi.org/10.1107/S0365110X57000134.

[55] W.P. Davey, Precision Measurements of the Lattice Constants of Twelve Common Metals, Phys. Rev. 25 (1925), 753. Doi: https://doi.org/10.1103/PhysRev.25.753.

[56] E. V. Shabunya-Klyachkovskaya, S. V. Gaponenko, S. V. Vaschenko, V. V. Stankevich, N. P. Stepina, A. S. Matsukovich, Plasmon Enhancement of Raman Scattering by Mercury Sulfide Microcrystals, J. Appl. Spectrosc. 81 (2014), 399-403. Doi: https://doi.org/10.1007/s10812-014-9944-3.

[57] G. Schmid, U. Simon, Gold nanoparticles: assembly and electrical properties in 1-3 dimensions, Chem. Commun. (2005), 697-710. Doi: https://doi.org/10.1039/B411696H.

[58] N.R. Devi, M. Sasidharan, A.K. Sundramoorthy, Gold Nanoparticles-Thiol-Functionalized Reduced Graphene Oxide Coated Electrochemical Sensor System for Selective Detection of Mercury Ion, J. Electrochem. Soc. 165 (2018), B3046-B3053. Doi: https://doi.org/10.1149/2.0081808jes.

[59] S.B.D. Borah, T. Bora, S. Baruah, J. Dutta, Heavy metal ion sensing in water using surface plasmon resonance of metallic nanostructures, Groundw. Sustain. Dev. 1 (2015), 1-11. Doi: https://doi.org/10.1016/j.gsd.2015.12.004.